In-gas-cell laser resonance ionization spectroscopy of ^{200,201}Pt

Y. Hirayama [1,*] M. Mukai,[2] Y. X. Watanabe [1] P. Schury [1] H. Nakada [3] J. Y. Moon [4] T. Hashimoto,[4]
S. Iimura [2,5] S. C. Jeong,[1] M. Rosenbusch,[1] M. Oyaizu,[1] T. Niwase [1] M. Tajima [2] A. Taniguchi,[6]
M. Wada,[1] and H. Miyatake [1]

[1]*Wako Nuclear Science Center (WNSC), Institute of Particle and Nuclear Studies (IPNS), High Energy
Accelerator Research Organization (KEK), Wako, Saitama 351-0198, Japan*
[2]*RIKEN Nishina Center for Accelerator-Based Science, RIKEN, Wako, Saitama 351-0198, Japan*
[3]*Department of Physics, Graduate School of Science, Chiba University, Inage, Chiba 263-8522, Japan*
[4]*Rare Isotope Science Project, Institute for Basic Science (IBS), Daejeon 305-811, Republic of Korea*
[5]*Department of Physics, Osaka University, Toyonaka, Osaka 563-0043, Japan*
[6]*Institute for Integrated Radiation and Nuclear Science, Kyoto University (KURNS), Kumatori, Osaka 590-0494, Japan*

The KEK Isotope Separation System (KISS) was used to produce neutron-rich platinum group isotopes via multinucleon transfer reactions. Mass-spectrometry-assisted in-gas-cell laser resonance ionization spectroscopy was utilized to perform the first experimental determinations of the magnetic dipole moment μ and the differential mean-square charge radii $\delta\langle r^2\rangle^{198,A}$ of ^{200,201}Pt. The quadrupole deformation parameters $|\langle\beta_2^2\rangle|^{1/2}$ were evaluated from the measured $\delta\langle r^2\rangle^{198,A}$ of ^{200,201}Pt by using a droplet model. The β_2 values were estimated from a comparison of the experimentally determined magnetic dipole moment μ with values calculated in a strong coupling model. Comparison of the $|\langle\beta_2^2\rangle|^{1/2}$ and β_2 values determined from the laser spectroscopy data with theoretical calculations indicates the likely spin-parity value for ^{201}Pt to be $I^\pi = 1/2^-$ or $5/2^-$.

I. INTRODUCTION

Laser spectroscopy is a proven tool for determining nuclear structure features [1]. The neutron-deficient and stable isotopes of lead [2,3], mercury [4–6], platinum [7–12], iridium [13,14], and osmium [15–18] have been well studied by laser spectroscopy. The isotope shifts $\delta\nu$, the differential mean-square charge radii $\delta\langle r^2\rangle$, and the quadrupole deformation parameter $|\langle\beta_2^2\rangle|^{1/2}$ have demonstrated shape staggering near mid-shell ($N \approx 104$) and shape transitions from prolate to oblate and then triaxial as the isotopes progress toward $N = 126$. These determinations of nuclear shape, in addition to the investigation of the magnetic dipole (μ) and electric quadrupole (Q) moments in this heavy region, provide good benchmarks for theoretical nuclear models. Unfortunately, however, there are almost no experimental data for the neutron-rich isotopes of the refractory elements with atomic numbers $Z = 70$–78 due to the immense difficulty in their production.

As a solution to the difficult production of these refractory elements, we have developed the KEK Isotope Separation System (KISS) [19–21]. Isotopes of Pt, Ir, Os, Re, W, and Ta approaching $N = 126$ [21] can be produced with reasonable yields by multinucleon transfer (MNT) reactions [22] with a primary beam of ^{136}Xe impinging on targets of ^{198}Pt, $^{\text{nat.}}$Pt, and $^{\text{nat.}}$W [23]. KISS provides Z and A separation to allow

precision studies (β- and γ-decay spectroscopy, half-life determinations, and mass measurements) of these neutron-rich nuclides. The MNT products are stopped in an argon-filled gas cell where they are neutralized. Gas flow transports the neutral atoms to a laser interaction region where in-gas-cell two-color two-step resonance laser ionization selectively ionizes atoms of the element we are interested in. The re-ionized beam is extracted by gas flow and transported through a differentially pumped region into high vacuum by RF multipole ion guides, then statically accelerated to 20 keV. A dipole magnet is then used to provide A/q selection and thereby provide a reasonably purified, singly charged ion beam of the desired neutron-rich nuclide [20]. We have previously reported the successful performance of such laser ionization spectroscopy for $^{199g,199m}_{78}$Pt [12], $^{196,197,198}_{77}$Ir [14], and $^{194,196}_{76}$Os [18].

For nuclides with sufficiently short lifetimes and sufficiently high yields, laser ionization spectroscopy can combine with decay spectroscopy to measure the hyperfine structure (HFS) spectrum. However, if the yield is too low or the lifetime is too long, then contamination from nonresonantly ionized isobars can impede the use of decay spectroscopy. To overcome this impediment we have implemented a multireflection time-of-flight mass spectrograph (MRTOF-MS) with sufficient resolving power to separate the neutron-rich nuclides of interest from the more stable isobars [24]. With such MRTOF-assisted laser spectroscopy, the yield as a function of laser wavelength can be determined without the need to observe decay radiations [18].

*yoshikazu.hirayama@kek.jp

We previously reported on laser spectroscopy of ^{199g,199m}Pt [12] which indicated a trend toward constancy in the quadrupole deformation parameter ($|\langle \beta_2^2 \rangle|^{1/2} \approx 0.14$ deduced from the measured $\delta \langle r^2 \rangle$ values by using the droplet model of Myers and Schmidt [25] for $N \geqslant 115$. This trend is similar to laser spectroscopic observations of $N \geqslant 119$ in the mercury isotopic chain [4], in contradiction to the observation of a trend toward reduced $|\langle \beta_2^2 \rangle|^{1/2}$ values as N approaches 126 deduced from $B(E2)$ measurements (references in Ref. [4]). To help clarify the general behavior, here we report our most recent work to extend laser spectroscopy of Pt toward $N = 126$ by utilizing MRTOF-assisted resonance laser ionization to perform the first such measurements of ^{200}Pt [$I^\pi = 0^+$ and $T_{1/2} = 12.6(3)$ h] [26] and ^{201}Pt [$I^\pi = (5/2^-)$ and $T_{1/2} = 2.5(1)$ min] [26]. The experimental results suggest that the likely spin-parity of ^{201}Pt is $I^\pi = 1/2^-$, $3/2^-$, or $5/2^-$ after accounting for the $\nu 3p_{1/2}$, $\nu 3p_{3/2}$, or $\nu 2f_{5/2}$ neutron orbits, respectively, under the neutron magic number $N = 126$. We evaluated $|\langle \beta_2^2 \rangle|^{1/2}$ values from the measured $\delta \langle r^2 \rangle^{198,A}$ in the context of a droplet model of Berdichevsky and Tondeur [27] which provides better mean-square charge radii near stability than those calculated by using the droplet model of Myers and Schmidt [25]. As another approach to deduce the β_2 values, we evaluated the values from a comparison of measured and calculated magnetic dipole moments in the context of a strong coupling model [28]. The $|\langle \beta_2^2 \rangle|^{1/2}$ and β_2 values evaluated by using both methods were compared with the theoretical values.

II. EXPERIMENT

The experiment was performed at the RIKEN Nishina Center for Accelerator-based Science. The RIKEN Ring Cyclotron was used to accelerate a 50 particle nA beam of ^{136}Xe to 10.75 MeV/nucleon. The ^{136}Xe primary beam impinged upon an enriched ^{198}Pt (91.63% purity) target with a thickness of 12.5 mg/cm^2. The resultant MNT products [23] were delivered to the argon-filled KISS gas cell wherein they were largely neutralized. The neutral atoms were quickly transported by gas flow to a laser-interaction region beyond which any re-ionized particles were transferred to vacuum, statically accelerated to 20 keV, and transported to the detector station via a mass-selective dipole magnet. The re-ionized particles were analyzed in an MRTOF-MS to quantify the rates of ^{198,200,201}Pt.

A. Ar gas cell for laser ionization

The unstable nuclei ^{200,201}Pt produced via MNT reactions, along with elastically scattered particles of stable ^{198}Pt, were emitted from the target and were injected into the doughnut-shaped argon gas cell [20]. The gas cell was maintained at room temperature and pressurized to 67 kPa for stopping and neutralizing the ^{200,201}Pt nuclei efficiently. The doughnut-shaped gas cell structure was designed to minimize plasma effects by allowing the ^{136}Xe primary beam to pass through an evacuated central axis while the elastically scattered particles and MNT products, being emitted at large angles, enter the gas cell through a thin doughnut-shaped window and are stopped by interactions with the argon gas and quickly neutralized. Any non-neutralized portion of the injected beam, along with any beam-induced ions, are suppressed by a set of ion-collection electrodes installed just upstream of the laser ionization region. The design of the gas-filled region has been optimized to provide efficient gas-flow transport of the unstable ions to a laser-interaction region near the exit of the gas cell [20]. By utilizing a two-step resonant laser ionization technique, atoms of the nuclide of interest can be re-ionized in a Z-selective fashion, then transported to a downstream analysis station via ion optical techniques. By systematically varying the laser wavelengths, the hyperfine structure of the nuclide of interest can be probed by in-gas-cell laser ionization spectroscopy.

The laser ionization spectroscopy is performed using a resonant excitation followed by a nonresonant ionizing transition to the continuum above the ionization potential (IP). For the resonant excitation ($\lambda_1 \approx 248.792$ nm) a XeCl excimer laser ($\lambda = 308$ nm, Lambda Physik LPX240i) was used to pump a tunable dye laser (Radiant Dyes Laser; NarrowScan) with a laser power of 100 μJ/pulse. For the nonresonant ionizing transition to the continuum ($\lambda_2 = 308$ nm), another XeCl excimer laser providing 12 mJ/pulse was used. The atomic transition between the ground state $5d^9 6s^3 D_3$ and the excited state $5d^8 6s 6p^5 F_4^0$, which was applied in our previously reported work [12], was studied by scanning the wavelength λ_1 to perform in-gas-cell laser ionization spectroscopy. The excimer lasers were operated at a repetition rate of 100 Hz and synchronized by a master trigger signal. To produce the deep UV laser beam at λ_1, the laser radiation from the NarrowScan laser was frequency doubled using a barium borate crystal placed in a second-harmonic generator. The typical line width of dye lasers was 3.4 GHz while their pulse width was 15 ns. The wavelength λ_1 was monitored by a WS6 wavemeter (HighFinesse) which had been precisely calibrated using a WS7-30 wavemeter (HighFinesse). Both laser beams had beam waists of 8–10 mm in diameter and were transported to the gas cell along paths which met in the gas cell at a small angle; the two beams were well overlapped at the ionization region of the gas cell and had appropriate temporal separation. The spatial overlap and temporal separation were monitored and maintained throughout the measurements.

B. Multireflection time-of-flight mass spectrograph station

The singly charged platinum ions (^{198,200,201}Pt$^+$) were statically accelerated to 20 keV after being extracted from the gas cell and transferred to high-vacuum. A single set of isobaric ions (hereafter referred to as the KISS beam) was selected by mass-to-charge ratio (A/q) using a dipole magnet and delivered to the MRTOF-MS station installed at the analysis station. The MRTOF-MS station comprises a gas-cell-based ion cooler (GCCB) [29], a suite of three RF ion traps, and an MRTOF-MS which itself consists of a pair of ion mirrors separated by a field-free drift region and followed by an ion impact detector (MagneTOF, ETP).

The GCCB efficiently converts the 20 keV KISS beam into a low-energy ion beam amenable to ion trapping. The GCCB is filled with helium gas and pressurized to $P \approx 100\,\mathrm{Pa}$ at room temperature. The KISS beam enters the GCCB through a 3 mm diameter entrance orifice after passing through a differentially pumped region in the front of the GCCB. Ionizing and elastic collisions with the buffer gas eventually thermalize the incoming KISS beam. After the thermalization, the KISS beam ions are transported by a static electric field along the length of the GCCB and extracted through a 1.28 mm exit orifice via an RF carpet. Due to electron stripping from the collisions with the helium gas, elements whose second IP is below helium's first IP [30] have been observed to be dominantly extracted as doubly charged ions (i.e., $^{200}\mathrm{Pt}^{2+}$); any incoming molecular ions undergo collision-induced dissociation.

A multi pole RF ion guide transports the thermalized ions to a linear Paul trap where the ions are accumulated and further cooled. This linear Paul trap is one of three RF ion traps used to prepare ions for analysis in the MRTOF-MS [31]. While the ions from the KISS beam are accumulating and cooling, reference ions from a rubidium thermal ion source are accumulated and cooled in a matching linear Paul trap. Between these two linear Paul traps is an RF ion trap of novel flat geometry ("flat trap") which can accept ions from two directions and ejects ions orthogonally to send them to the MRTOF-MS for analysis.

A typical MRTOF-MS analysis cycle is composed of two 25 ms in duration subcycles: one for reference ions and the other for analyte ions. For 95% of the analysis cycle, KISS beam ions accumulate in a linear Paul trap. The analyte subcycle begins when a 1 ms duration transfer phase moves KISS beam ions from the linear Paul trap to the flat trap, where they are cooled for 5 ms before being injected into the MRTOF-MS. Once in the MRTOF-MS, the ions of interest are allowed to reflect for a time sufficient to make 350 laps back and forth (about 6 ms flight time), then the bias applied to the mirror electrode nearest the ion impact detector is adjusted to allow ions to leave the analyzer and travel to the detector. The reference subcycle follows a similar pattern, but it starts with a transfer phase moving reference ions from their linear Paul trap. The time-of-flight spectra produced during the present measurements exhibited a mass resolving power of $\Delta m/m = 80\,000$, which was sufficient to identify the $^{200,201}\mathrm{Pt}^{2+}$ using multipeak fitting based on the reference ion's spectral peak shape.

C. Principle of laser ionization spectroscopy

Laser ionization spectroscopy is a powerful method to study nuclear structure. The nuclear electromagnetic moments and the differential mean-square charge radii can be deduced as nuclear-model-independent quantities from the investigation of hyperfine (HF) levels governed by the quantum number $F \in [|I - J|, I + J]$, where I and J are the nuclear and atomic spins, respectively. In terms of the F values, if $I, J \geqslant 1/2$, the nominally degenerate atomic energy levels resolve by shifting in energy:

$$\Delta E = \frac{A}{2} K_{\mathrm{HFS}} + \frac{B}{2} \frac{C}{2I(2I-1)2J(2J-1)},$$
$$C = 3K_{\mathrm{HFS}}(K_{\mathrm{HFS}}+1) - 2I(I+1)2J(J+1),$$
$$K_{\mathrm{HFS}} = F(F+1) - I(I+1) - J(J+1), \tag{1}$$

where A and B are the magnetic-dipole and electric-quadrupole HF coupling constants, respectively.

A and B are proportional to the nuclear magnetic dipole moment μ and nuclear electric quadrupole moment Q, respectively, and can be written as

$$A = \frac{\mu H_{JJ}(0)}{IJ}, \tag{2}$$

$$B = eQ\phi_{JJ}(0) \quad (I, J \geqslant 1), \tag{3}$$

where $H_{JJ}(0)$ and $\phi_{JJ}(0)$ are the magnetic field and electric field gradients, respectively, which are induced by the atomic electrons at the position of the nucleus. While $H_{JJ}(0)$ and $\phi_{JJ}(0)$ are specific to each atomic state, they are common across all the nuclides of an element. Thus, a nuclide's nuclear electromagnetic moments can be evaluated from its measured A and B values by using any set of known A', B', I', μ', and Q' for another nuclide of the same element (generally a stable nuclide) as follows:

$$\mu = \frac{I}{I'} \frac{A}{A'} \mu' \tag{4}$$

and

$$Q = \frac{B}{B'} Q' \quad (I, J \geqslant 1). \tag{5}$$

The shifts in the atomic energies of the ground and excited states, ΔE_{gs} and ΔE_{ex}, respectively, occur as a result of HF interactions between the nucleus and atomic electrons. The shifts in the transition frequency for excitation between the HF levels of the ground and excited states are

$$\Delta \nu_i = \Delta E_{i:\mathrm{ex}} - \Delta E_{i:\mathrm{gs}} \tag{6}$$

relative to the center of gravity of the fine-structure transition frequency ν_0. From laser spectroscopy measurements of the HF splitting term $\Delta \nu_i$ values, the HF coupling constants A and B—and, by extension, the electromagnetic moments μ and Q—can be determined.

Among platinum isotopes, the nuclide $^{195}\mathrm{Pt}$ ($I^\pi = 1/2^-$ and $\mu = +0.609\,49(6)\mu_{\mathrm{N}}$ [32]) has been reported to have HF coupling constants $A_{\mathrm{gs}} = 5.702\,64(23)\,\mathrm{GHz}$ [33] and $A_{\mathrm{ex}} = 1.14(7)\,\mathrm{GHz}$ [12] for the atomic ground state ($5d^9 6s\,^3D_3$) and excited state ($5d^8 6s6p\,^5F_4^0$), respectively. The HF coupling constant B_{gs} for the atomic ground state in platinum has been reported to be being given by $B_{\mathrm{gs}} = -Q/0.685\,\mathrm{GHz}$ [9]. In the analyses of HFS spectra in this work, the unknown HF coupling constant B_{ex} for the atomic excited state was treated as a free parameter.

III. DATA ANALYSIS

Analysis of the mass-spectrometry-assisted laser ionization measurements is a two-step process. Initially, the relative
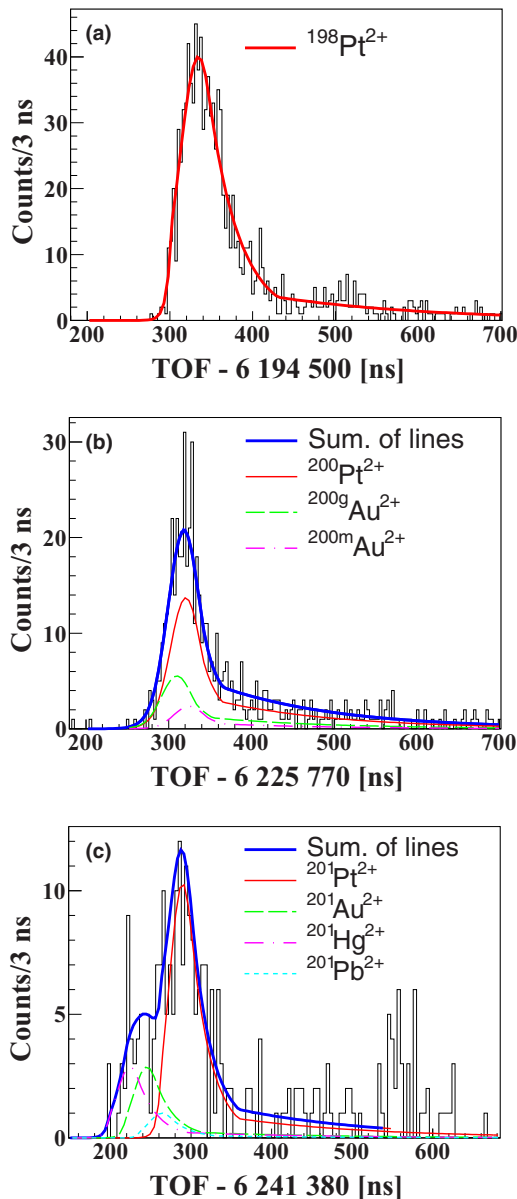
FIG. 1. Typical TOF spectra for ions with mass-to-charge ratios of (a) $A/q = 99$, (b) $A/q = 100$, and (c) $A/q = 100.5$ after $n = 350$ laps in the MRTOF-MS. The blue (thick solid) lines show the total fit function, the red (thin solid) lines indicate the platinum ion contribution to the spectral peaks, and other colors indicate contributions from nonresonantly ionized isobars. Each TOF datum was taken at the ionization maximum.

intensity of the nuclide of interest must be determined from the time-of-flight spectra recorded using the MRTOF-MS. These data can then be used to produce laser resonance spectra which can be analyzed to extract various information.

A. Identification of ^{198,200,201}Pt and evaluation of their rates from time-of-flight spectra

Figures 1(a), 1(b), and 1(c) show typical TOF spectra obtained during the laser ionization spectroscopy measurements. The spectrum in Fig. 1(a) is a single-component spectral peak

of ^{198}Pt^{2+}, while Figs. 1(b) and 1(c) show multicomponent spectral peaks for $A/q = 100$ and 100.5, respectively. Based on the spectral peak shape of ^{198}Pt^{2+}, a Gaussian-exponential hybrid with a two-component slow tail [18] was chosen for the fitting function, and can be seen to reproduce the data quite well. The tail features are presumed to result from higher-order optical aberrations in mirror electrodes of MRTOF-MS and low-angle scattering from collisions with residual gas in the MRTOF-MS [34].

Due to the low mass-resolving power available during this work, the ^{200}Pt^{2+} and ^{201}Pt^{2+} spectral peaks included contributions from nonresonant ionized isobars. As all these nuclides have well-known atomic masses [35], it was possible to make a multipeak fitting to extract the ^{200,201}Pt^{2+} contributions, despite them being unresolved, by fixing the relative times of flight based on the known atomic masses. The peak shape parameters—Gaussian width and exponential-tail parameters—were fixed based on the results of fitting a high-statistics ^{198}Pt^{2+} spectral peak. The amplitudes of each nuclide's contribution to the spectral peaks were the only free parameters in these fittings. The fitting analyses were performed using the ROOT MINUIT library [36].

B. Laser resonance spectra of ^{198,200,201}Pt

As previously mentioned, TOF spectra were measured as functions of the excitation laser wavelength λ_1 for ^{198,200,201}Pt. In each measurement, as discussed in the previous section, there were also significant quantities of nonresonantly ionized isobars which contaminated the TOF spectra. The rate of these nonresonantly ionized contaminants was observed previously [18] and in this work to be fairly constant.

We considered two options to produce laser ionization response functions from the TOF spectra. For TOF spectra produced at laser wavelengths near the ionization maximum, it was possible to extract an amplitude for the platinum ions and determine the platinum rate from the area under the fitting curve; however, spectra produced further from the laser ionization spectral center had an insufficient contribution of platinum ions to ascertain a reliable amplitude. Alternatively, the contributions of the nonresonantly ionized isobars could be determined by fitting and subtracted from the total counts in each spectral peak. Unfortunately, due to their low rate—particularly so in the measurement of ^{201}Pt—error propagation leads to untenably large relative uncertainties outside the center of the laser ionization spectrum. Therefore, since these nonresonantly ionized contaminants were observed at a fairly constant rate, we opted to evaluate the laser ionization spectrum with a constant offset as shown in Fig. 2.

The spectra shown in Fig. 2 were produced by counting the total ions in the region of the platinum ions. The observed peak shape of ^{198}Pt^{2+} and the contaminants identified in the TOF spectra of ^{200}Pt^{2+} and ^{201}Pt^{2+} were used to select appropriate counting ranges for each isotope. In the cases of ^{198}Pt^{2+} and ^{200}Pt^{2+} a range of $t \in [t_c - 100$ ns, $t_c + 400$ ns] was chosen, where t_c is the expected TOF peak position of the platinum ions. For ^{201}Pt^{2+} a range of $t \in [t_c - 40$ ns, $t_c + 80$ ns] was selected to maximally exclude the partially resolved contaminants. To account for fluctuations in laser power, timing,
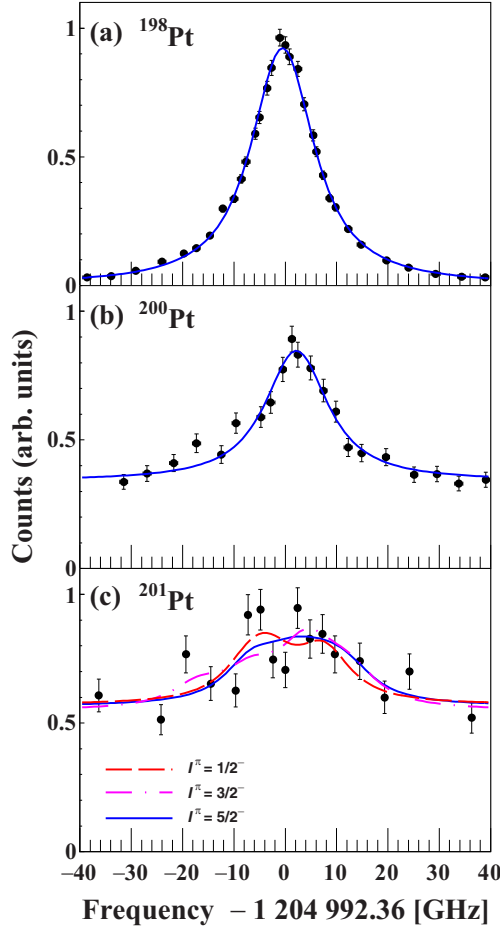
FIG. 2. Laser resonance spectra of (a) ^{198}Pt, (b) ^{200}Pt, and (c) ^{201}Pt determined by MRTOF-assisted ionization spectroscopy. In the case of ^{201}Pt, fitting curves are shown for three possible spin-parity values: $I^\pi = 1/2^-$, $3/2^-$, and $5/2^-$. The fitting curves are shown as solid or dashed lines, with the best fits being the solid blue lines.

and position an additional 3% systematic uncertainty was added to the statistical uncertainties.

C. Fitting analyses of laser resonance spectra

The response function for the present in-gas-cell laser ionization spectroscopy measurements of platinum isotopes was determined by analyzing the laser resonance spectrum of ^{198}Pt ($I^\pi = 0^+$) measured in the same online experiment as ^{200,201}Pt, as shown in Fig. 2(a). The line shape is a Voigt function, which is a convolution of Gaussian and Lorentzian components. The Gaussian width is composed of two components—the laser line width and Doppler broadening—which must be added in quadrature. The laser linewidth is 3.4 GHz full width at half maximum (FWHM) while Doppler broadening due to the 300 K argon gas is 1.0 GHz FWHM, producing a total Gaussian width of 3.5 GHz, which is a fixed parameter for analysis of all three nuclides. The response function in this work is governed mainly by its Lorentzian components which are derived from gas-pressure broadening, laser-power broadening, and

Nuclide	I^π	$\delta\nu_{\exp}^{198,A}$ (GHz)	$\mu_{\exp}$ (μ_N)	Q (b)	Reduced χ^2
^{198}Pt	0^+	2.43(23)[a]	N/A	N/A	N/A
^{199}Pt	$5/2^-$	2.13(41)[a]	+0.75(8)[a]	+1.7(17)[a]	N/A
^{200}Pt	0^+	2.69(41)	N/A	N/A	1.19
^{201}Pt	$1/2^-$	2.31(135)	+0.44(7)	N/A	0.96
	$3/2^-$	0.35(134)	−0.83(15)	−2.7(45)	0.98
	$5/2^-$	4.20(171)	+0.86(21)	+1.0(39)	0.99

[a]Previously measured values [12]. For the case of ^{198}Pt, the isotope shift value is expressed as $\delta\nu_{\exp}^{194,198}$.

the 63 MHz natural linewidth of the transition. Fitting of the ^{198}Pt data gave a Lorentzian width of $\Gamma_L = 13.9(3)$ GHz.

The resultant best fit to the data, based on the common Gaussian and Lorentzian widths evaluated from the ^{198}Pt spectrum, are shown for ^{200}Pt and ^{201}Pt in Figs. 2(b) and 2(c), respectively. From these fits, it was possible to determine the magnetic dipole moment μ and isotope shifts $\delta\nu^{198,A}$ ($A = 200, 201$) relative to the peak of the ^{198}Pt resonance curve. The uncertainties in the determination of physical quantities such as $\delta\nu^{198,A}$, μ, and Q were determined through appropriate consideration of the covariance matrix in the fitting routine and standard error propagation methods, by performing simultaneous fits to the spectra pairs in Figs. 2(a)–2(b) and 2(a)–2(c). In the fitting routine for the ^{200}Pt case, the free parameters were Γ_L, $\delta\nu^{198,200}$, amplitude, and background level.

Another important parameter is the amplitude of each HF transition peak for the case of ^{201}Pt. The present line width ≈ 14 GHz was much broader than the HF energy shift ($\leqslant 5$ GHz). Therefore, the relative intensity [37] for each transition can be applied in the analysis [12,14] to reduce the number of free parameters and constrain the amplitude. The peak height of each transition between the ith HF level ($F_{gs,i}$) in the ground state and the kth HF level ($F_{ex,k}$) in the excited state is calculated from the statistical weight ($2F + 1$) of each HF level (F). It is given by

$$\frac{2F_{gs,i}+1}{\Sigma_j(2F_{gs,j}+1)} \frac{2F_{ex,k}+1}{\Sigma_l(2F_{ex,l}+1)} \times f_{amp}, \tag{7}$$

where $F_{gs,j}$ and $F_{ex,l}$ are the total angular momentum of the jth HF level in the ground state and lth HF level in the excited state, respectively. The $F_{ex,l}$ levels can be populated from $F_{gs,i}$ by the excitation laser due to the broad line width. The f_{amp} value is a common coefficient for all transitions to fit the HFS spectrum of ^{201}Pt, and is treated as one of the free parameters. Finally, for the case of spectrum analysis of ^{201}Pt, the free parameters are Γ_L, $\delta\nu^{198,201}$, μ, Q, B_{ex}, f_{amp}, and background.

The blue solid lines indicate the best fit to each spectrum as shown in Figs. 2(a), 2(b), and 2(c). The present fitting analyses were also performed by using the ROOT MINUIT library [36]. The fitting results are summarized in Table I. In the

case of ^{201}Pt, spin-parity I^π is unknown, and, therefore, the simultaneous fit to the spectra in Figs. [2(a)]–[2(c)] was performed for each of the three cases of $I^\pi = 1/2^-$, $3/2^-$, and $5/2^-$, by accounting for the expected neutron orbits of $3p_{1/2}$, $3p_{3/2}$, and $2f_{5/2}$ under $N = 126$.

IV. RESULTS AND DISCUSSION

The difference between the mean-square charge radius of a nucleus of ^{A}Pt and that of ^{198}Pt, $\delta\langle r^2\rangle^{198,A}$, can be calculated directly from a measured isotope shift $\delta\nu^{198,A}$ without nuclear model dependence. The magnetic dipole moment μ can be deduced from the HFS spectrum, albeit with a dependence on spin-parity. Additionally, the deformation parameter $|\langle\beta_2^2\rangle|^{1/2}$ can be calculated from the difference in charge radius by use of a droplet model; it has been shown that the Berdichevsky and Tondeur model [27] provides more reliable mean-square charge radii near stability than those calculated by using the Myers and Schmidt model [25]. We also evaluated β_2 values of ^{199,201}Pt from the comparison between the measured magnetic dipole moment $\mu_{\exp}$ and the $\mu_{\rm cal}$ value calculated by a strong coupling model [28] as another point of view. Here we will present the values of these physical quantities deduced from laser ionization spectroscopy measurements and discuss their implications.

A. Isotope shift, differential mean-square charge radius, and deformation parameters of ^{200}Pt and ^{201}Pt

After fitting the measured laser resonance ionization curves, the isotope shift for ^{200}Pt was determined to be $\delta\nu^{198,200} = +2.69 \pm 0.41$ GHz, as listed in Table I. As the spin-parity of ^{201}Pt is uncertain, its isotope shift determination is more complicated as it must be determined for multiple assumed spin-parity values. The isotope shifts determined based on $I^\pi = 1/2^-$, $3/2^-$, and $5/2^-$ are also shown in Table I. While isotope shifts $\delta\nu^{198,201}$ evaluated assuming $I^\pi = 1/2^-$ or $5/2^-$ follow the expected systematic trend of linearly increasing trend toward $N = 126$ as previously reported for lead [2] and mercury [4] isotopic chains, the isotope shift evaluated assuming $I^\pi = 3/2^-$ would be in violation of such systematics.

The isotope shifts were then used to evaluate the differential mean-square charge radii $\delta\langle r^2\rangle^{198,A}$ in a nuclear-model-free methodology. The difference in isotope shift between two nuclides of mass numbers A and A' can be expressed as

$$\delta\nu^{A,A'} = (K_{\rm NMS} + K_{\rm SMS}) \times \frac{m_{A'} - m_A}{m_{A'}m_A} + F_{248} \times \delta\langle r^2\rangle^{A,A'}, \quad (8)$$

where $K_{\rm NMS}$ and $K_{\rm SMS}$ are the factors for the normal and specific mass shifts, respectively, while $F_{248} \times \delta\langle r^2\rangle^{A,A'}$ is the first-order term in the field shift. The electronic factor F_{248} is specific to the transition $\lambda_1 = 248.792$ nm, and $\delta\langle r^2\rangle^{A,A'}$ is the isotopic variation of the mean-square charge radius. The field shift terms of higher order in differential mean-square charge radius represent less than 5% of the field shift and can be neglected for our purposes.

TABLE II. Measured differential mean-square charge radii $\delta\langle r^2\rangle^{198,A}$ and calculated deformation parameters $\langle\beta_2^2\rangle$ determined for platinum isotopes. The values for ^{200,201}Pt are from this work while those for ^{198,199}Pt are from previous work [12] to provide the reader insight into systematic trends.

Nuclide	I^π	$\delta\langle r^2\rangle^{194,A}$ (fm²)	$\|\langle\beta_2^2\rangle\|^{1/2}$
^{198}Pt	0^+	0.143(20)[a]	0.100(9)
^{199}Pt	$5/2^-$	0.268(34)[a]	0.122(12)
^{200}Pt	0^+	0.295(30)	0.107(11)
^{201}Pt	$1/2^-$	0.287(81)	0.073(45)
	$3/2^-$	0.172(79)	
	$5/2^-$	0.398(104)	0.120(35)

[a]Previously measured values [12].

To determine the differential mean-square charge radius, we rearrange Eq. [8] to

$$\delta\langle r^2\rangle^{A,A'} = \frac{\delta\nu^{A,A'}}{F_{248}} - \frac{K_{\rm NMS} + K_{\rm SMS}}{\alpha \cdot F_{248}}, \quad (9)$$

where $\alpha = \frac{m_{A'}m_A}{m_{A'} - m_A}$. The mass shift is only a few tens of MHz [38], while the field shift factor F_{248} was evaluated to be 17.0 ± 1.8 GHz/fm² in previous measurements [12]. Within the precision of our measurements we can safely neglect the second term in Eq. [9] [12]. The resultant differential mean-square charge radii values derived from such calculations are provided in the third column of Table II.

Figure [3] shows the differential mean-square charge radii of the platinum isotope [9,11,12] as a function of neutron number. It is expected that the nuclear shape will tend toward spherical near $N = 126$, leading to a linear trend in differential mean-square charge radii as previously reported for lead [2] and mercury [4] isotopic chains. For ^{201}Pt, the differential mean-square charge radii determined assuming $I^\pi = 1/2^-$ and $5/2^-$ are consistent with such a linear trend. As was similarly observed for the isotope shift value, an assumption of $I^\pi = 3/2^-$ yields a value that is inconsistent with a presumed linear trend.

The experimentally determined mean-square charge radius can be approximated as

$$\langle r^2\rangle_{\exp}^A = \langle r^2\rangle_{\rm sph}^A + \frac{5}{4\pi}\langle r^2\rangle_{\rm sph}^A\langle\beta_2^2\rangle^A, \quad (10)$$

where $\langle r^2\rangle_{\exp}^A$ and $\langle r^2\rangle_{\rm sph}^A$ are the experimentally determined and spherical components of the nuclear mean-square charge radius of ^{A}Pt, respectively, while $\langle\beta_2^2\rangle^A$ is the quadrupole deformation parameter for ^{A}Pt. It was previously demonstrated [9,39] that Eq. [10] can be rewritten such that the quadrupole deformation parameter can be evaluated from the differential mean-square charge radius by

$$\langle\beta_2^2\rangle^A = \frac{\delta\langle r^2\rangle_{\exp}^{194,A} - \delta\langle r^2\rangle_{\rm sph}^{194,A}}{\frac{5}{4\pi}\langle r^2\rangle_{\rm sph}^A} + \frac{\langle r^2\rangle_{\rm sph}^{194}\langle\beta_2^2\rangle^{194}}{\langle r^2\rangle_{\rm sph}^A}. \quad (11)$$

To use Eq. [11] for evaluating the $\langle\beta_2^2\rangle^A$ values of ^{200,201}Pt from the laser spectroscopy data acquired in this work, the $\langle r^2\rangle_{\rm sph}^A$ and $\delta\langle r^2\rangle_{\rm sph}^{194,A}$ values were calculated using the Berdichevsky and Tondeur droplet model [27], which is
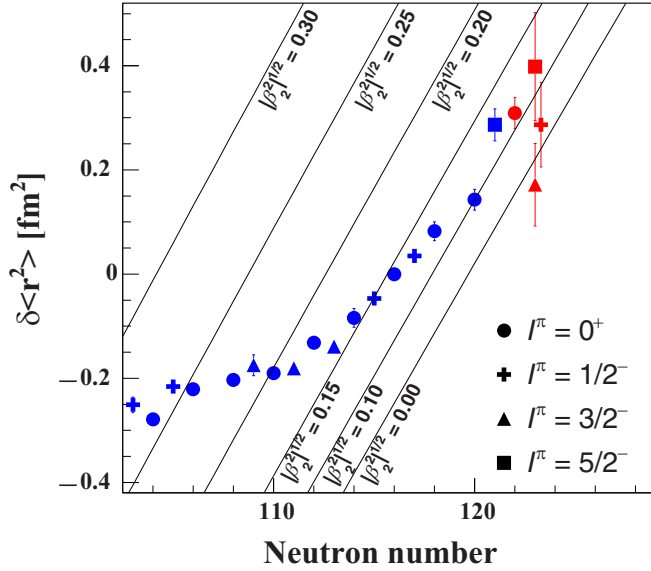
FIG. 3. Differential mean-square charge radii of platinum isotopes, determined from isotope shift measurements [9,12], presented as a function of neutron number N. The symbol shape indicates the spin-parity values used in fitting the laser spectroscopy data from which the isotope shift was determined. Data represented with blue symbols were derived from Refs. [9,12], while red symbols are data derived from this work. Data are superimposed on lines of constant quadrupole deformation parameters based on a normalization to $|\langle \beta_2^2 \rangle|^{1/2}(^{194}\text{Pt}) = 0.1434$ evaluated from precise $B(E2)$ measurements of ^{194}Pt.

known to reliably estimate the spherical component of the nuclear charge radius. As the quadrupole deformation parameters for even $A \leqslant 198$ platinum nuclei deduced from the precisely measured $B(E2, 2^+ \rightarrow 0^+)$ values are known to yield reliable results [40], they were used for the normalization value $\langle \beta_2^2 \rangle^{194}$. The resulting absolute deformation parameters $|\langle \beta_2^2 \rangle|^{1/2}$ for $^{198,199,200,201}\text{Pt}$ are listed in Table II. The value for ^{201}Pt with an assumed spin-parity of $3/2^-$ is not listed. It yielded an unphysical negative value, leading us to exclude $I^\pi = 3/2^-$ as a likely spin-parity for ^{201}Pt.

To better evaluate the trend of quadrupole deformation parameters in the platinum isotopic chain, calculated $|\langle \beta_2^2 \rangle|^{1/2}$ lines are included in Fig. 3. In our previous work [12] we evaluated the quadrupole deformation parameters for $^{193-199}\text{Pt}$ ($115 \leqslant N \leqslant 121$) based on the Myers and Schmidt droplet model [25], concluding that the $|\langle \beta_2^2 \rangle|^{1/2}$ values among those nuclides were constant, ≈ 0.14. A similar but less pronounced behavior can be seen now using the Berdichevsky and Tondeur droplet model, with the quadrupole deformation slowly trending from $|\langle \beta_2^2 \rangle|^{1/2} = 0.15$ to $|\langle \beta_2^2 \rangle|^{1/2} \approx 0.1$ as the neutron number passes $N = 120$. The $|\langle \beta_2^2 \rangle|^{1/2}$ value for ^{200}Pt derived from laser ionization spectroscopy in this work continues the trend, as do those for ^{201}Pt assuming $I^\pi = 1/2^-$ or $5/2^-$.

It is worth noting that a similar trend of relatively constant $|\langle \beta_2^2 \rangle|^{1/2}$ values for the neutron-rich mercury isotope ($N \geqslant 117$) was reported [4] based on measured $B(E2)$ values. However, at even higher N, approaching the $N = 126$ shell closure, the $|\langle \beta_2^2 \rangle|^{1/2}$ values decreased [4], indicative of a

spherical nuclear shape at the shell closure. With this in mind, it must be noted that Eqs. (10) and (11) might be imprecise nearer to the shell closure [4] or in the case of sizable octupole and hexacapole deformations.

B. Magnetic dipole moment of ^{201}Pt

For the HFS spectrum shown in Fig. 2(c), the fits were made for three possible spin-parity values of $I^\pi = 1/2^-$, $3/2^-$, and $5/2^-$, and from each a magnetic dipole moment μ for $^{201}\text{Pt}_{123}$ was deduced. The results are shown in Table I. Due to the broad resonance width of the present in-gas-cell laser ionization spectroscopy method it is not possible to determine the spin-parity value from the reduced χ^2 values of the fits; consequently we cannot uniquely determine the magnetic dipole moment. The evaluation of the quadrupole moment, however, is largely insensitive to different spin-parity values due to a very large relative uncertainty as a consequence of the quadrupole moment being responsible for a much smaller HF energy shift than the magnetic dipole moment [12].

Another way to determine the likely spin-parity value of ^{201}Pt is to make systematic comparisons with known magnetic dipole moments of nearby nuclides with the assumption that, among nearby nuclides, the magnetic dipole moment should be largely conserved for a given spin-parity value. Considering $I^\pi = 1/2^-$, we find that $^{205}\text{Hg}_{125}$ and $^{207}\text{Pb}_{125}$ have a magnetic dipole moment $\mu \approx 0.60 \ \mu_N$, carried by a $3p_{1/2}$ valence neutron [41], which is a 2.3σ deviation from the magnetic dipole moment deduced for ^{201}Pt assuming $I^\pi = 1/2^-$. In the unlikely case of $I^\pi = 3/2^-$ we have only $^{201}\text{Hg}_{121}$ as a point of comparison; the reported value of $\mu = -0.560\ 225\ 7(14)\mu_N$ [42] differs by 1.8σ from the value we derive for ^{201}Pt assuming $I^\pi = 3/2^-$. The first $I^\pi = 5/2^-$ states in $^{195,197,199}\text{Pt}$ and $^{197,199,203}\text{Hg}$ all have $\mu \approx +0.8\mu_N$ [43], while ^{203}Hg—an isotone of ^{201}Pt—has a magnetic dipole moment $\mu = +0.848\ 95(3)\mu_N$, carried by a $2f_{5/2}$ valence neutron, which is in excellent agreement with the value we deduce for ^{201}Pt assuming $I^\pi = 5/2^-$.

C. Alternate evaluation of the deformation parameter β_2 in a strong-coupling model

In order to determine the possible spin-parity value and deformation parameter β_2 of ^{201}Pt based on the magnetic dipole moment μ_{exp}, a theoretical magnetic dipole moment μ_{cal} for ^{201}Pt was calculated as a function of the β_2 value for the three cases of $I^\pi = 1/2^-$, $3/2^-$, and $5/2^-$ by using Eqs. (12) and (13) in the strong coupling model [28]:

$$\mu_{\text{cal}} = g_R I + (g_K - g_R)\frac{K^2}{I+1} \quad (K > 1/2), \qquad (12)$$

$$\mu_{\text{cal}} = g_R I + \frac{(g_K - g_R)}{4(I+1)}[1 + (2I+1)(-1)^{I+1/2}b]$$
$$(K = 1/2), \qquad (13)$$

where $g_R = Z_{\text{core}}/A_{\text{core}}$ and g_K are the g factors associated with the collective motion of the nuclear core and with the

individual particle motions in the deformed nucleus, respectively, while b is the magnetic decoupling parameter given by Eq. (4) (A-12) of Ref. [28]. The projection of the nuclear spin onto the deformation symmetry axis is given by K; for the nuclear ground state, $K = I$.

We can express g_K as

$$g_K = \frac{1}{K}[g_\ell K + (g_s - g_\ell)\langle K \mid \hat{s}_3 \mid K \rangle] \quad (K \neq 1/2),$$

$$(g_K - g_R)b = -(g_\ell - g_R)a - \frac{1}{2}(-1)^\ell(g_s + g_K - 2g_\ell)$$

$$(K = 1/2),$$

where g_s and g_ℓ are the spin and orbital g factors associated with the motion of a valence nucleon, while $\hat{s}_3$ is the nucleon spin operator along the deformation symmetry axis and a is the rotational decoupling parameter given in Eq. (5)-46 in Ref. [28].

As the valence nucleon in $^{\text{odd}}$Pt nuclei is a neutron, when considering ^{201}Pt we set $g_s = 0.75 \times g_s^{\text{free}}$ ($g_s^{\text{free}} = -3.826$) as recommended in the heavy-mass region [44] and set $g_\ell = 0$. The values of $\langle K \mid \hat{s}_3 \mid K \rangle$, b, and a were calculated using a theoretical model which describes energy eigenstates of the nucleus as one particle plus core in the axially symmetric quadrupole-deformed potential [45]. The calculation requires a value for β_2 as an input parameter to describe the axially symmetric quadrupole-deformed potential, and thereby we were able to calculate μ_{cal} as a function of the β_2 value.

To confirm the reliability of the model calculation we began by calculating μ_{cal} as a function of β_2 for the $I^\pi = 5/2^-$ nuclide $^{203}_{80}\text{Hg}_{123}$. Interpolating between the reported β_2 values of ^{202,204}Hg in Ref. [4], we could expect $\beta_2 = -0.075$. We find that $\mu_{\text{cal}} = \mu_{\text{exp}}$ when $\beta_2 = -0.054$, which is sufficiently similar to the expected value to validate the methodology.

Figures 4(a), 4(c), and 4(e) show the calculated magnetic dipole moment as functions of β_2 for $I^\pi = 1/2^-$, $3/2^-$, and $5/2^-$, respectively. Figures 4(b), 4(d), and 4(f) provide the calculated probabilities as functions of β_2 for the various single-particle wavefunctions used in the calculation of μ_{cal}. The negative β_2 values are expected from the systematic trend and suggested by various theoretical calculations [46–48]. In order to gauge the effect of a small variance in the effective spin g factor of the valence nucleon, the magnetic dipole moment was calculated within a conservative range of $\delta g_s = \pm 0.05$ for each spin-parity option. As can be seen from Figs. 4(a), 4(c), and 4(e), the effect of such a variation is small.

In order to extract the β_2 value from these calculations, the experimentally determined magnetic dipole moment is included in Figs. 4(a), 4(c), and 4(e), where the solid black lines denote the central value and the error band is indicated by the dashed lines. We deduce the β_2 value to be where the central value of μ_{exp} crosses the μ_{cal} curves, with an error band given by the μ_{exp} error band's intersection with the μ_{cal} curves. In the case of $I^\pi = 1/2^-$ we can only obtain a lower limit of $\beta_2 \geqslant -0.10$, while in the case of $I^\pi = 3/2^-$ there is no crossing observed for $\beta_2 \leqslant 0$. However, we could not exclude the possibility of the $I^\pi = 3/2^-$ assignment from the magnetic dipole moment because the μ_{cal} value with the
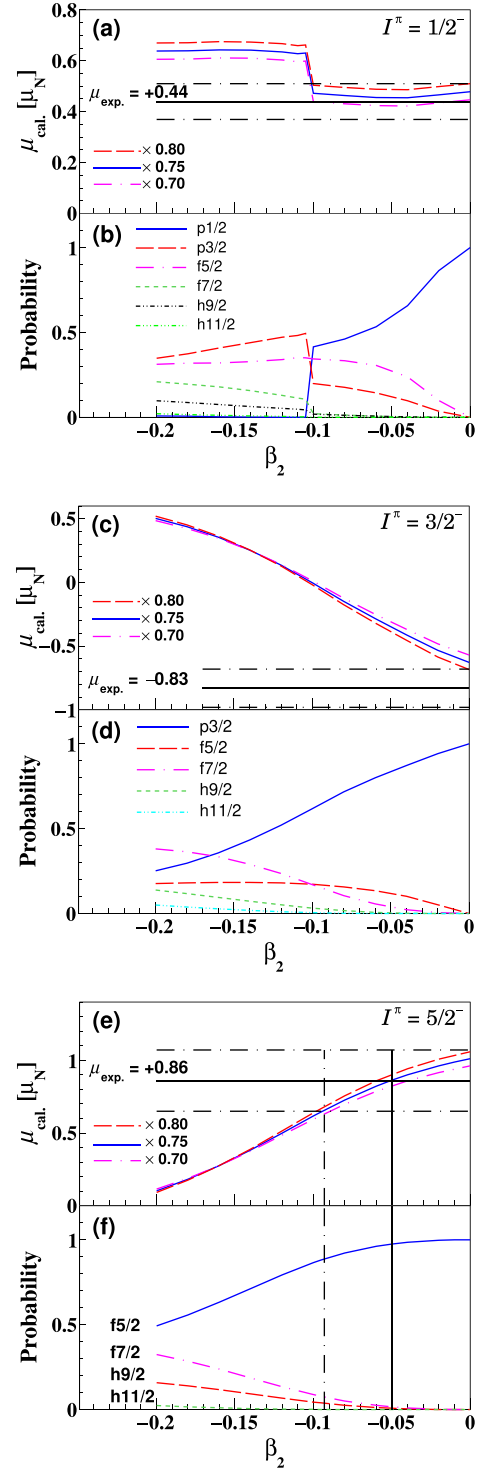

FIG. 4. Calculated μ_{cal} value of ^{201}Pt with (a) $I^\pi = 1/2^-$, (c) $I^\pi = 3/2^-$, and (e) $I^\pi = 5/2^-$ by using the strong coupling model [45] as a function of β_2 value. Here, we calculated μ_{cal} values by applying the effective $g_s^{\text{eff.}} = f \times g_s^{\text{free}}$ ($f = 0.7, 0.75,$ and 0.8). The calculated probability of each neutron orbit in the ground state of ^{201}Pt with (b) $I^\pi = 1/2^-$, (d) $I^\pi = 3/2^-$, and (f) $I^\pi = 5/2^-$ by using the strong coupling model [45] as a function of β_2 value. The horizontal black solid and dotted lines indicate the measured μ_{exp} values and their uncertainties, respectively, for the cases of $I^\pi = 1/2^-$, $3/2^-$, and $5/2^-$.

TABLE III. Comparison of quadrupole deformation parameters from this work with those from theoretical calculations. Under "This work" the $|\langle\beta_2^2\rangle|^{1/2}$ are derived from Eq. (11) using the Berdichevsky and Tondeur droplet model, while the β_2 values are deduced from the application of a strong coupling model.

Nuclide	This work		SCCM+Gogny D1S	FRDM	CHFB-5DSC
	$|\langle\beta_2^2\rangle|^{1/2}$ from $\delta\nu$	β_2 from μ_{exp}	[46]	[47]	+Gogny D1S[48]
^{198}Pt	0.100(9)		−0.11	−0.115	$\approx$−0.12
^{199}Pt	0.122(12)	$-0.077^{+0.017}_{-0.014}$		−0.115	$\sim$− 0.12
^{200}Pt	0.107(11)		−0.05	−0.084	$\sim$− 0.09
^{201}Pt ($I^\pi = 1/2^-$)	0.073(45)	$-0.10\leqslant$		−0.073	$\sim$− 0.08
^{201}Pt ($I^\pi = 5/2^-$)	0.120(35)	$-0.05^{+0.05}_{-0.045}$		−0.073	$\sim$− 0.08
^{202}Pt			−0.05<	−0.063	$\sim$0.0
^{203}Pt				0.000	$\sim$0.0
^{204}Pt			0.00	0.000	$\sim$0.0

lower β_2 is approaching the μ_{exp} value by accounting for the experimental uncertainty. In the case of $I^\pi = 5/2^-$, however, we find $\beta_2 = -0.05^{+0.05}_{-0.045}$, where the large relative uncertainty is a consequence of the large uncertainty in μ_{exp}. While this value is less than half the $|\langle\beta_2^2\rangle|^{1/2}$ value determined previously from the isotope shift and droplet model, the two values are consistent in considering the large error bars. In light of our earlier evaluation of the spin-parity of ^{201}Pt in terms of systematic trends in the magnetic dipole moment, it is worth noting that the oblately deformed $2f_{5/2}$ state contributes the dominant wave function in this calculation.

The same analysis was applied to the nuclide ^{199}Pt, indicating $\beta_2 = -0.077^{+0.017}_{-0.014}$ based on the previously measured $\mu_{\text{exp}} = +0.75(8)$ μ_N [12]. This deviates more than 2σ from the value we obtained using isotope shift data and the nuclear droplet model. Nonetheless, considering the β_2 values of ^{198,199,201}Pt we see the expected tendency for $\beta_2 \to 0$ when approaching $N = 126$.

As shown in Table III, we compared the deduced $|\langle\beta_2^2\rangle|^{1/2}$ values with various theoretical β_2 values calculated by using symmetry-conserving configuration-mixing (SCCM) with Gogny D1S energy density functionals [46], finite range droplet model (FRDM) [47], and the constrained-Hartree-Fock-Bogoliubov (CHFB) theory with five-dimensional collective Hamiltonian (5DCH) based on the Gogny D1S interaction [48]. The three calculations show that the oblately-deformed shape for the $^{198-202}$Pt nuclei approaches the spherical shape as we approach to the $N = 126$ closed shell; the exception being the CHFB − 5DSC+Gogny D1S calculation.

The $|\langle\beta_2^2\rangle|^{1/2}$ values of ^{198,199}Pt, which were calculated from the measured isotope shifts by using the droplet model [27], agree with the theoretical calculations [46–48] listed in Table III. The $|\langle\beta_2^2\rangle|^{1/2}$ values of ^{200,201}Pt deduced from the isotope shifts by using the droplet model [27] are consistent with the theoretical β_2 values. The β_2 values evaluated from the measured μ_{exp} by using the strong coupling model [28], for the cases of ^{199,201}Pt, are also consistent with the theoretical values. These β_2 values show the systematic tendency of shape changing from oblate to spherical shape toward the $N = 126$ closed shell. Finally, the present $|\langle\beta_2^2\rangle|^{1/2}$ values deduced from Eq. (11) with the use of the droplet model of

Berdichevsky and Tondeur [27] and the present β_2 values from the comparison between μ_{exp} and μ_{cal} values obtained by using the strong coupling model [28] are consistent with the theoretical values.

V. SUMMARY

Laser spectroscopy has proven to be a powerful tool by which we can deduce nuclear properties such as differential mean-square charge radii and magnetic dipole moments. We have measured the isotope shifts $\delta\nu$ for the neutron-rich nuclei ^{200}Pt [$I^\pi = 0^+$ and $T_{1/2} = 12.6(3)$ h] and ^{201}Pt [$T_{1/2} = 2.5(1)$ min] by performing in-gas-cell laser resonance ionization spectroscopy using an MRTOF-MS to identify and count the resonantly ionized ions. The application of the MRTOF-MS allows the laser resonance ionization technique to be extended to both extremely low-yield and long-lived species of unstable nuclei.

Using a nuclear-model-independent analysis, we were able to deduce the differential mean-square charge radii of ^{200,201}Pt from the measured isotope shifts. Since ^{200}Pt has $I^\pi = 0$ and no HFS, the differential mean-square charge radius $\delta\langle r^2\rangle^{198,200} = 0.295(30)$ fm^2 could be unambiguously determined. In the case of ^{201}Pt, however, the spin-parity value is unknown but presumed to be $I^\pi = 1/2^-$, $3/2^-$, or $5/2^-$, resulting in $\delta\langle r^2\rangle^{198,201} = 0.287(81)$ fm^2, 0.172(79) fm^2, or 0.398(104) fm^2, respectively. Similarly, for $I^\pi = 1/2^-$, $3/2^-$, or $5/2^-$ we found the magnetic dipole moment to be $\mu = +0.44(7)\mu_N$, $-0.83(15)\mu_N$, or $+0.86(21)\mu_N$, respectively. By systematic comparison with the $\mu = +0.848\,95(3)\mu_N$ moment of the isotone ^{203}Hg$_{123}$ with $I^\pi = 5/2^-$ originating from neutron orbit $2f_{5/2}$, we found that the most likely spin-parity would be $I^\pi = 5/2^-$, while the other two options are excluded at the 2σ level.

Using the Berdichevsky and Tondeur droplet model, which has demonstrated improved accuracy over the previously used Myers and Schmidt model, we evaluated the quadrupole deformation parameters. For ^{200}Pt we evaluated $|\langle\beta_2^2\rangle|^{1/2} = 0.107(11)$ using the differential mean-square charge radius determined from the isotope shift and spherical contributions to the charge radius from the improved droplet model. As with the magnetic dipole moment, the quadrupole deformation

parameter for ^{201}Pt was evaluated for each possible spin-parity, yielding $|\langle\beta_2^2\rangle|^{1/2} = 0.073(45)$ or $0.120(35)$ for $I^\pi = 1/2^-$ or $5/2^-$, respectively, while evaluation for $I^\pi = 3/2^-$ yielded an unphysical negative value. The evaluation reasonably excluded $I^\pi = 3/2^-$ as a possible spin-parity for ^{201}Pt.

Another evaluation of the β_2 value of ^{201}Pt was performed in the context of a strong coupling model [28] to further probe the likely spin-parity. Before applying the strong coupling model to ^{201}Pt we confirmed that the methodology yielded correct results for ^{203}Hg and ^{199}Pt. In the case of $I^\pi = 1/2^-$, evaluation in the context of the strong coupling model could only set a lower limit of $\beta_2 \geqslant -0.10$, while in the case of $I^\pi = 5/2^-$ the deformation parameter was determined to be $\beta_2 = -0.05^{+0.05}_{-0.045}$. The deformation parameters determined by either method generally agree with the trend seen in theoretical calculations based on SCCM, FRDM, and CHFB-5DSC, i.e., the tendency toward $\beta_2 = 0$ as the isotopic chain approaches the closed neutron shell at $N = 126$, indicative of a spherical shape.

Considering the evaluation of the magnetic dipole moment in a systematic context, along with the evaluation of the quadrupole deformation parameter by multiple methodologies, we can reasonably exclude the spin-parity $I^\pi = 3/2^-$ for ^{201}Pt. In light of these various analyses, it seems that the most likely candidate would be $I^\pi = 5/2^-$. However, it is not possible to exclude $I^\pi = 1/2^-$ as a possible spin-parity of ^{201}Pt.

In order to advance our understanding of the nuclear structure in the vicinity of the neutron closed shell at $N = 126$ we plan to continue our systematic study of neutron-rich refractory elements such as Pt, Ir, Os, Re, W, and Ta at KISS using resonance laser ionization spectroscopy. We continue to improve upon the technique, such as by utilizing an MRTOF-MS to identify the ions. We continue to improve the performance of the MRTOF-MS, both in terms of mass resolution and overall efficiency, to allow us to reach ever more exotic nuclides. Furthermore, we have been using state-of-the-art laser systems combined with a narrow-band technique to develop a capability for in-gas-jet laser ionization spectroscopy [21,49] which should dramatically reduce the width of the resonance ionization spectra and greatly improve our ability to determine isotope shifts, magnetic moments, and spin-parity values.

[1] P. Campbell, I. Moore, and M. Pearson, Prog. Part. Nucl. Phys. **86**, 127 (2016).

[2] R. Thompson, M. Anselment, K. Bekk, S. Goring, A. Hanser, G. Meisel, H. Rebel, G. Schatz, and B. Brown, J. Phys. G **9**, 443 (1983).

[3] H. De Witte, A. N. Andreyev, N. Barrè, M. Bender, T. E. Cocolios, S. Dean, D. Fedorov, V. N. Fedoseyev, L. M. Fraile, S. Franchoo, V. Hellemans, P. H. Heenen, K. Heyde, G. Huber, M. Huyse, H. Jeppessen, U. Köster, P. Kunz, S. R. Lesher, B. A. Marsh *et al.*, Phys. Rev. Lett. **98**, 112502 (2007).

[4] G. Ulm, S. Bhattacherjee, P. Dabkiewicz, G. Huber, H.-J. Kluge, T. Kühl, H. Lochmann, E.-W. Otten, and K. Wendt, Z. Phys. A **325**, 247 (1986).

[5] B. Marsh, T. D. Goodacre, S. Sels, Y. Tsunoda, B. Andel, A. Andreyev, N. Althubiti, D. Atanasov, A. Barzakh, J. Billowes, K. Blaum, T. Cocolios, J. Cubiss, J. Dobaczewski, G. Farooq-Smith, D. Fedorov, V. Fedosseev, K. Flanagan, L. Gaffney, L. Ghys *et al.*, Nat. Phys. **14**, 1163 (2018).

[6] T. Day Goodacre, A. V. Afanasjev, A. E. Barzakh, B. A. Marsh, S. Sels, P. Ring, H. Nakada, A. N. Andreyev, P. Van Duppen, N. A. Althubiti, B. Andel, D. Atanasov, J. Billowes, K. Blaum, T. E. Cocolios, J. G. Cubiss, G. J. Farooq-Smith, D. V. Fedorov, V. N. Fedosseev, K. T. Flanagan *et al.*, Phys. Rev. Lett. **126**, 032502 (2021).

[7] J. K. P. Lee, G. Savard, J. E. Crawford, G. Thekkadath, H. T. Duong, J. Pinard, S. Liberman, F. Le Blanc, P. Kilcher, J. Obert, J. Oms, J. C. Putaux, B. Roussière, and J. Sauvage, Phys. Rev. C **38**, 2985 (1988).

[8] H. Duong, J. Pinard, S. Liberman, G. Savard, J. Lee, J. Crawford, G. Thekkadath, F. L. Blanc, P. Kilcher, J. Obert, J. Oms, J. Putaux, B. Roussière, J. Sauvage, and the ISOCELE Collaboration, Phys. Lett. B **217**, 401 (1989).

[9] T. Hilberath, S. Becker, G. Bollen, H.-J. Kluge, U. Krönert, G. Passler, J. Rikovska, R. Wyss, and the ISOLDE Collaboration, Z. Phys. A **342**, 1 (1992).

[10] P. Kilcher, J. Putaux, J. Crawford, H. Dautet, H. Duong, F. L. Blanc, J. Lee, J. Obert, J. Oms, J. Pinard, B. Roussière, J. Sauvage, G. Savard, and G. Thekkadath, Nucl. Instrum. Methods Phys. Res. Sect. B **70**, 537 (1992).

[11] F. Le Blanc, D. Lunney, J. Obert, J. Oms, J. C. Putaux, B. Roussière, J. Sauvage, S. Zemlyanoi, J. Pinard, L. Cabaret, H. T. Duong, G. Huber, M. Krieg, V. Sebastian, J. E. Crawford, J. K. P. Lee, M. Girod, S. Péru, J. Genevey, and J. Lettry (ISOLDE Collaboration), Phys. Rev. C **60**, 054310 (1999).

[12] Y. Hirayama, M. Mukai, Y. X. Watanabe, M. Ahmed, S. C. Jeong, H. S. Jung, Y. Kakiguchi, S. Kanaya, S. Kimura, J. Y. Moon, T. Nakatsukasa, M. Oyaizu, J. H. Park, P. Schury, A. Taniguchi, M. Wada, K. Washiyama, H. Watanabe, and H. Miyatake, Phys. Rev. C **96**, 014307 (2017).

[13] D. Verney, L. Cabaret, J. Crawford, H. Duong, B. Fricke, J. Genevey, G. Huber, F. Ibrahim, M. Krieg, F. L. Blanc, J. Lee, G. L. Scornet, D. Lunney, J. Obert, J. Oms, J. Pinard, J. Puteaux,

K. Rashid, B. Roussière, J. Sauvage *et al.*, Eur. Phys. J. A **30**, 489 (2006).

[14] M. Mukai, Y. Hirayama, Y. X. Watanabe, S. Schiffmann, J. Ekman, M. Godefroid, P. Schury, Y. Kakiguchi, M. Oyaize, M. Wada, S. C. Jeong, J. Y. Moon, J. H. Park, H. Ishiyama, S. Kimura, H. Ueno, M. Ahmed, A. Ozawa, H. Watanabe, S. Kanaya, and H. Miyatake, Phys. Rev. C **102**, 054307 (2020).

[15] A. Hines and J. Ross, Phys. Rev. **126**, 2105 (1962).

[16] P. Aufmuth and E. Wöbker, Z. Phys. A **321**, 65 (1985).

[17] S. Kröger, A. B. G. Basar, and G. Guthöhrlein, Phys. Scr. **65**, 56 (2002).

[18] H. Choi, Y. Hirayama, S. Choi, T. Hashimoto, S. C. Jeong, H. Miyatake, J. Y. Moon, M. Mukai, T. Niwase, M. Oyaizu, M. Rosenbusch, P. Schury, A. Taniguchi, Y. X. Watanabe, and M. Wada, Phys. Rev. C **102**, 034309 (2020).

[19] Y. Hirayama, Y. Watanabe, N. Imai, H. Ishiyama, S. Jeong, H. Miyatake, M. Oyaizu, S. Kimura, M. Mukai, Y. H. Kim, T. Sonoda, M. Wada, M. Huyse, Y. Kudryavtsev, and P. V. Duppen, Nucl. Instrum. Methods Phys. Res. Sect. B **353**, 4 (2015).

[20] Y. Hirayama, Y. Watanabe, M. Mukai, M. Oyaizu, M. Ahmed, H. Ishiyama, S. Jeong, Y. Kakiguchi, S. Kimura, J. Moon, J. Park, P. Schury, M. Wada, and H. Miyatake, Nucl. Instrum. Methods Phys. Res. Sect. B **412**, 11 (2017).

[21] Y. Hirayama, Y. Watanabe, M. Mukai, P. Schury, M. Ahmed, H. Ishiyama, S. Jeong, Y. Kakiguchi, S. Kimura, J. Moon, M. Oyaizu, J. Park, M. Wada, and H. Miyatake, Nucl. Instrum. Methods Phys. Res. Sect. B **463**, 425 (2020).

[22] C. H. Dasso, G. Pollarolo, and A. Winther, Phys. Rev. Lett. **73**, 1907 (1994).

[23] Y. X. Watanabe, Y. H. Kim, S. C. Jeong, Y. Hirayama, N. Imai, H. Ishiyama, H. S. Jung, H. Miyatake, S. Choi, J. S. Song, E. Clement, G. de France, A. Navin, M. Rejmund, C. Schmitt, G. Pollarolo, L. Corradi, E. Fioretto, D. Montanari, M. Niikura *et al.*, Phys. Rev. Lett. **115**, 172503 (2015).

[24] J. Moon, T. Hashimoto, S. Jeong, M. Wada, P. Schury, Y. Watanabe, Y. Hirayama, Y. Ito, M. Rosenbusch, T. Niwase, H. Wollnik, and H. Miyatake, RIKEN Accel. Prog. Rep. **53**, 128 (2019).

[25] W. Myers and K.-H. Schmidt, Nucl. Phys. A **410**, 61 (1983).

[26] http://www.nndc.bnl.gov.

[27] D. Berdichevsky and F. Tondeur, Z. Phys. A **322**, 141 (1985).

[28] A. Bohr and B. Mottelson, *Nuclear Structure Volume II: Nuclear Deformations* (World Scientific, Singapore, 1988).

[29] J. Moon, S. Jeong, M. Wada, P. Schury, Y. Watanabe, Y. Hirayama, Y. Ito, M. Rosenbusch, S. Kimura, S. Ishizawa, T. Niwase, H. Wollnik, and H. Miyatake, RIKEN Accel. Prog. Rep. **52**, 138 (2018).

[30] P. Schury, T. Hashimoto, Y. Ito, H. Miyatake, J. Moon, T. Niwase, Y. Hirayama, M. Rosenbusch, M. Wada, Y. Watanabe, and H. Wollnik, RIKEN Accel. Prog. Rep. **53**, 115 (2019).

[31] P. Schury, M. Wada, Y. Ito, D. Kaji, F. Arai, M. MacCormick, I. Murray, H. Haba, S. Jeong, S. Kimura, H. Koura, H. Miyatake, K. Morimoto, K. Morita, A. Ozawa, M. Rosenbusch, M. Reponen, P.-A. Söderström, A. Takamine, T. Tanaka *et al.*, Phys. Rev. C **95**, 011305(R) (2017).

[32] R. Firestone, *Table of Isotopes* (John Wiley & Sons, New York, 1996).

[33] S. Büttgenbach, N. Glaeser, B. Roski, and R. Träber, Z. Phys. A **317**, 237 (1984).

[34] Y. Ito, P. Schury, M. Wada, S. Naimi, T. Sonoda, H. Mita, F. Arai, A. Takamine, K. Okada, A. Ozawa, and H. Wollnik, Phys. Rev. C **88**, 011306(R) (2013).

[35] M. Wang, W. Huang, F. Kondev, G. Audi, and S. Naimi, Chin. Phys. C **45**, 030003 (2021).

[36] CERN Program Library entry D506.

[37] U. Köster, N. J. Stone, K. T. Flanagan, J. R. Stone, V. N. Fedosseev, K. L. Kratz, B. A. Marsh, T. Materna, L. Mathieu, P. L. Mokkanov, M. D. Seliverstov, O. Serot, A. M. Sjödin, and Y. M. Volkov, Phys. Rev. C **84**, 034320 (2011).

[38] K. Blaum, J. Dilling, and W. Nörtershäuser, Phys. Scr. **2013**, 014017 (2013).

[39] S. Ahmad, W. Klempt, C. Ekström, R. Neugart, K. Wendt, and the ISOLDE collaboration, Z. Phys. A **321**, 35 (1985).

[40] S. Raman, J. Nestor, S. Kahane, and K. Bhatt, At. Data Nucl. Data Tables **42**, 1 (1989).

[41] J. Rodriguez, J. Bonn, G. Huber, H.-J. Kluge, and E. Otten, Z. Phys. A **272**, 369 (1975).

[42] R. Reimann and M. McDermott, Phys. Rev. C **7**, 2065 (1973).

[43] N. J. Stone, At. Data Nucl. Data Tables **90**, 75 (2005).

[44] S. Pèru, S. Hilaire, S. Goriely, and M. Martini, Phys. Rev. C **104**, 024328 (2021).

[45] I. Hamamoto, Phys. Rev. C **99**, 024319 (2019).

[46] P. John, J. Valiente-Dobón, D. Mengoni, V. Modamio, S. Lunardi, D. Bazzacco, A. Gadea, C. Wheldon, T. Rodríguez, T. Alexander, G. de Angelis, N. Ashwood, M. Barr, G. Benzoni, B. Birkenbach, P. Bizzeti, A. Bizzeti-Sona, S. Bottoni, M. Bowry, A. Bracco *et al.*, Phys. Rev. C **95**, 064321 (2017).

[47] P. Möller, A. Sierk, T. Ichikawa, and H. Sagawa, At. Data Nucl. Data Tables **109-110**, 1 (2016).

[48] J.-P. Delaroche, M. Girod, J. Libert, H. Goutte, S. Hilaire, S. Péru, N. Pillet, and G. F. Bertsch, Phys. Rev. C **81**, 014303 (2010).

[49] Y. Kudryavtsev, R. Ferrer, M. Huyse, P. V. den Bergh, and P. V. Duppen, Nucl. Instrum. Methods Phys. Res. Sect. B **297**, 7 (2013).